Publications

1-2017

First Performance Results of a New Field-Widened Spatial Heterodyne Spectrometer for Geocoronal Hα Research

D. D. Gardner
University of Wisconsin - Madison

E. J. Mierkiewicz
Embry-Riddle Aeronautical University, mierkiee@erau.edu

F. L. Roesler
University of Wisconsin - Madison

J. M. Harlander
Saint Cloud State University

K. P. Jaehnig
University of Wisconsin - Madison

See next page for additional authors

Scholarly Commons Citation

Authors

D. D. Gardner, E. J. Mierkiewicz, F. L. Roesler, J. M. Harlander, K. P. Jaehnig, S. M. Nossal, and L. M. Haffner

Key Points:
- FW-SHS instrument extends H alpha observations with high resolving power and long spectral baseline
- Field-widening prisms allow faint emission detection in compact instrumental design
- FW-SHS observations are consistent with WHAM observations and coincidentally obtained Fabry Perot observations

Correspondence to:
D. D. Gardner,
ddgardner@wisc.edu

First performance results of a new field-widened spatial heterodyne spectrometer for geocoronal Hα research

D. D. Gardner[1], E. J. Mierkiewicz[2], F. L. Roesler[1], J. M. Harlander[3], K. P. Jaehnig[1], S. M. Nossal[1], and L. M. Haffner[1,4]

[1]University of Wisconsin-Madison, Madison, Wisconsin, USA, [2]Embry-Riddle Aeronautical University-Daytona Beach, Daytona Beach, Florida, USA, [3]Saint Cloud State University, St. Cloud, Minnesota, USA, [4]Space Science Institute, Boulder, Colorado, USA

Abstract A new, high-resolution field-widened spatial heterodyne spectrometer (FW-SHS) designed to observe geocoronal Balmer α (Hα, 6563 Å) emission was installed at Pine Bluff Observatory (PBO) near Madison, Wisconsin. FW-SHS observations were compared with an already well-characterized dual-etalon Fabry-Perot Interferometer (PBO FPI) optimized for Hα, also at PBO. The FW-SHS is a robust Fourier transform instrument that combines a large throughput advantage with high spectral resolution and a relatively long spectral baseline (~10 times that of the PBO FPI) in a compact, versatile instrument with no moving parts. Coincident Hα observations by FW-SHS and PBO FPI were obtained over similar integration times, resolving powers (~67,000 and 80,000 at Hα) and fields of view (1.8° and 1.4°, respectively). First light FW-SHS observations of Hα intensity and temperature (Doppler width) versus viewing geometry (shadow altitude) show excellent relative agreement with the geocoronal observations previously obtained at PBO by FPI. The FW-SHS has a 640 km/s (14 Å) spectral band pass and is capable of determining geocoronal Hα Doppler shifts on the order of 100 m/s with a temporal resolution on the order of minutes. These characteristics make the FW-SHS well suited for spectroscopic studies of relatively faint (~12–2 R), diffuse-source geocoronal Hα emission from Earth's upper thermosphere and exosphere and the interstellar medium in our Galaxy. Current and future FW-SHS observations extend long-term geocoronal hydrogen observation data sets already spanning three solar minima. This paper describes the FW-SHS first light performance and Hα observational results collected from observing nights across 2013 and 2014.

1. Introduction

A novel interferometer for remote sensing upper thermospheric and exospheric temperatures and dynamics, referred to as a field-widened spatial heterodyne spectrometer (FW-SHS), has recently been built and field tested at Pine Bluff Observatory, WI. The first use of FW-SHS for observations of geocoronal Balmer α (Hα, 6563 Å) airglow and diffuse Galactic Hα recombination emission are compared here to coincidently obtained Fabry-Perot Hα observations. The purpose of this paper is to show how FW-SHS geocoronal observations are calibrated and consistent with Hα observations obtained by Fabry-Perot and thus illustrate the precision with which this FW-SHS can contribute to Hα intensity, temperature, and Doppler shift observations from the Earth's outer atmosphere and our Galaxy.

Ground-based hydrogen airglow observations as forward model constraints to atmospheric coupled radiative transport models of Hα allow retrieval and model comparison of relevant exospheric aeronomical parameters such as hydrogen density and temperature profiles and vertical hydrogen flux [e.g., *Bishop*, 2001; *Bishop et al.*, 2004]. Ground-based Hα observations serve as a unique geometrical constraint for these atmospheric parameters, and with multiple instruments at various latitudes these parameters' global variations can begin to be investigated.

Ground-based measurements of geocoronal airglow emission have historically been obtained by Fabry-Perot Interferometers, favored for etendue (throughput) and resolving power necessary to fully characterize this diffuse emission line profile. The unique instrumental characteristics of the FW-SHS instrument allow it to surpass Fabry-Perot Interferometers (FPI) in operational versatility and instantaneously sampled band-pass range at similar throughput and resolving powers [e.g., *Harlander et al.*, 1992; *Roesler and Harlander*, 1990].

The SHS in its most basic configuration is similar to a Michelson interferometer but with gratings replacing the mirrors in each arm, thus negating the need for mechanical scanning. Spectra are then obtained by
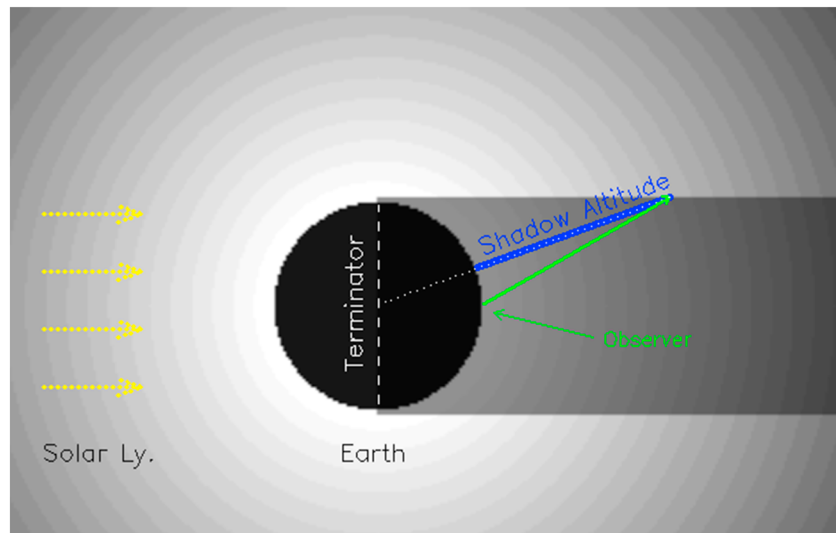
Figure 1. Observational viewing geometry illustrating shadow distance (green) and shadow altitude (blue) for an observer at local midnight. The Sun illuminates from the left, scattering off hydrogen and producing Balmer series fluorescence proportional to the H density; Earth's shadow falls to the right. Emission all along the line of sight contributes (as does the Galactic H_α background) to the H_α column emission. At deeper shadow altitudes, multiple scattering into Earth's shadow progressively dominates.

Fourier transform of the resulting Fizeau fringes imaged on a CCD detector. Matched dual field-widening prisms mounted in each arm further increase the etendue of the SHS, giving it an order-of-magnitude larger sensitivity, on par of that typically obtained by FPI's with a similar effective aperture. Additionally, the FW-SHS is easily transportable and boasts more relaxed optical-flatness defect tolerances than FPI's at similar wavelengths.

In this paper we begin with a basic overview of geocoronal H_α line emission, the FW-SHS instrumental concept, specifics of our interferometer, observational strategy, and data analysis. Next, we describe our method of spectral and photometric cross calibration for the FW-SHS interferometer using already established dual-etalon FPI instrumentation (Pine Bluff Observatory (PBO) FPI) and Northern Sky Survey data from the Wisconsin H_α Mapper (WHAM) [*Haffner et al.*, 2003]. We conclude with showing first light FW-SHS results obtained with coincident PBO FPI observations, demonstrating instrumental performance, ability to contribute to long-term ground-based geocoronal H_α data sets, and aid in retrieval of exospheric dynamical signatures.

2. Overview of the Geocoronal H_α Line Profile

Solar Lyman β flux scattering off atomic hydrogen in the upper thermosphere and exosphere generates geocoronal H_α fluorescence in a diffuse manner, filling the field of view (FOV) of our interferometers. As discussed in depth by *Mierkiewicz et al.* [2006], the nighttime H_α column emission rate ("intensity") observed from the ground depends on the strength of the Lyman β line center flux, the hydrogen density profile, and observational viewing geometry. At higher altitudes, as hydrogen density decreases, there is less H_α emission. Ground-based column emission observations capture geocoronal H_α emission originating from all along the line of sight.

Column emission observations are typically categorized by the shadow altitude geometry. Earth's shadow cylinder (illustrated in Figure 1) radius corresponds to the terminator altitudes where Lyman β radiation is fully attenuated by O_2 screening, ~102 km. As illustrated in Figure 1 by the blue line, the shadow *altitude* is then the radial vector (perpendicular) from ground to the observation point on Earth's shadow that also intersects the line-of-sight shadow *distance* (the green line in Figure 1) from a ground observer to the same observation point. Shadow altitude is uniquely determined by the observer's longitude, latitude and topocentric altitude, the direction to the target, and the time.

Low shadow altitude geocoronal H_α emission observations (e.g., dawn/dusk) are comparably brightest, being dominated by single scattering of solar Lyman β near the denser base of the total column emission. Typical FPI observations as a function of shadow altitude show geocoronal H_α intensities ranging from ~12 Rayleighs (R, here after) near the terminator (~400 km shadow altitude) down to ~2 R looking antisunward into Earth's shadow (>20,000 km shadow altitudes). Multiple scattering of solar Lyman β into Earth's shadow prevents observed geocoronal H_α intensities from approaching zero at high shadow altitudes.

Long-term PBO FPI data sets [*Mierkiewicz et al.,* 2006] of low shadow altitude (<5000 km) geocoronal H_α intensity measurements show a dawn/dusk asymmetry. Zenith dawn measurements are usually brighter by a few Rayleighs (~10–20%) than their dusk counterparts. There is also strong evidence for seasonal variation in H_α intensity [*Tinsley*, 1970] and H_α temperature [*Mierkiewicz et al.,* 2012]. Long-term (solar cycle) intensity trends and variations, by as much as ~50%, have been discussed in depth by *Nossal et al.* [1993, 2001, 2006, 2008]. Temporal intensity variations have been largely thought attributable [e.g., *Tinsley*, 1970; *Kerr et al.,* 2001] to fluctuations in exospheric distribution, content and production of hydrogen, and fluctuations in solar Lyman β line center strength.

The geocoronal H_α Doppler emission width is dominated by the temperature near the base of the column emission at the shadow altitude of observation, where the solar illuminated column has its highest density. However, the entire column emission contributes to the profile, and due to the range of hydrogen velocity distributions sampled along the column, the distribution is not strictly Maxwellian; therefore, temperatures derived from fitting the observed profiles as though they were Maxwellian are referred to as "effective temperatures." As a function of shadow altitude, the geocoronal H_α Doppler width is typically observed to narrow in a near linear fashion from ~7 km/s near the terminator to ~4 km/s at shadow altitudes near 20,000 km [*Mierkiewicz et al.,* 2012]. For hydrogen, this narrowing corresponds to a drop from ~850 K to ~400 K in the effective temperature probed by the H_α line width. *Kerr et al.* [1986] attributed this narrowing to gravitational cooling of hydrogen.

The spectral line profile of geocoronal H_α fluorescence originates primarily from two solar Lyman β directly excited fine-structure components that dominate the H_α intensity in a 2 to 1 ratio, along with seven fine-structure cascade transition components due to higher order solar Lyman excitation [*Meier*, 1995]. The overall geocoronal H_α line profile is inherently non-Gaussian. The dominant cascade transition $(3^2S_{1/2} \rightarrow 2^2P_{3/2})$ is redshifted by 6.3 km/s from the dominant directly excited transition $(3^2P_{3/2} \rightarrow 2^2S_{1/2})$. *Mierkiewicz et al.* [2006] showed that at low shadow altitudes (<5000 km) the cascade contributions account for 5% ($\pm$3)of the total observed geocoronal H_α emission intensity. At high resolving powers achieved by PBO FPI, *Nossal et al.* [1998] noted that the cascade contributions to geocoronal H_α line profile are not negligible, and *Roesler et al.* [2014] show that cascade can be constrained by the simultaneously observed intensity of H_β. When cascade is ignored, effective temperatures retrieved from fits can be overestimated by as much as ~10%.

While our PBO FPI and FW-SHS operate at comparable peak signal-to-noise ratios (SNR) for similar integration times, the FW-SHS longer spectral baseline allows the H_α background emission from the Galaxy to be better characterized and separated from geocoronal emission. Additionally, the presence of multiple thorium calibration lines across the FW-SHS band pass allows spectral registration and instrumental profile determination to be quite precise. Exospheric and Galactic spectral shifts are then readily calibrated by comparison against calibration lamp spectra taken in the laboratory (or observatory).

3. FW-SHS Instrumental Concept

The SHS concept [e.g., *Roesler and Harlander*, 1990; *Harlander et al.,* 1992; *Roesler et al.,* 2003] and variations [e.g., *Corliss et al.,* 2015; *Lawler et al.,* 2008] are now well described in the literature. Referring to Figure 2 now, we describe how the FW-SHS instrument works: Prefiltered night sky light is collimated through the input lens (A), split at the beam splitter (C), and passing through two matched field-widening prisms in nearly identical path-length arms (D_{1-4}), the light at frequencies around Littrow wave number, σ_0, is reflected and dispersed by gratings (G) to be recombined at the beam splitter (C), exiting through the first output lens (B) toward the CCD.
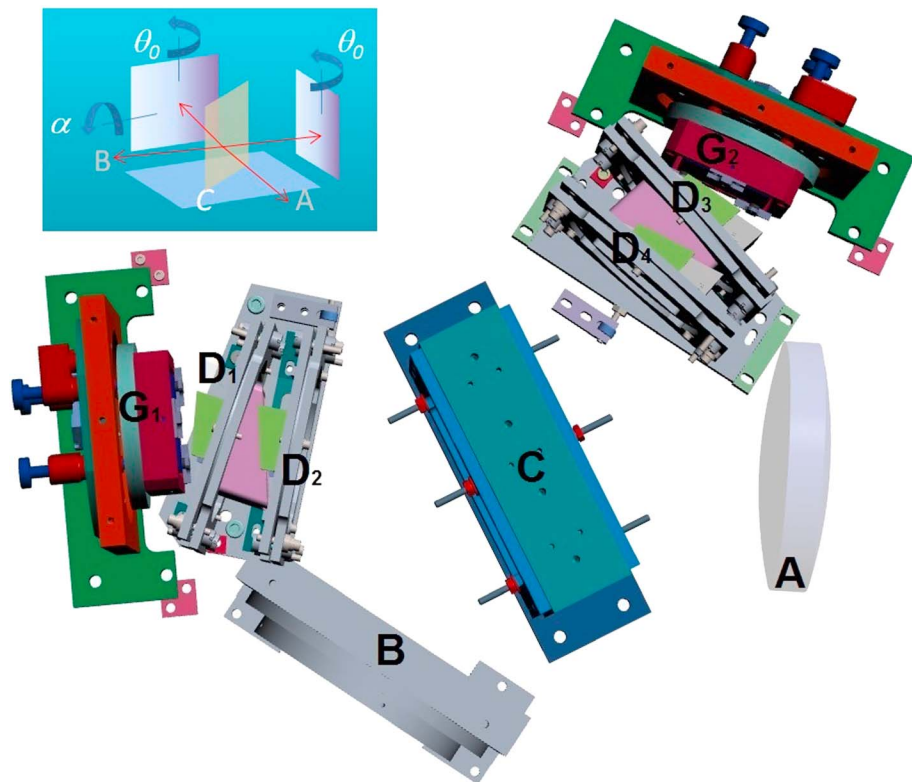
Figure 2. Solid works instrument model of our FW-SHS. Light enters through the collimating lens (A) on right, to be split at the beam splitter (C), recombined, and focused by output optics (B) to a CCD. *Two* prisms in *each* arm (D_{1-4}) maximize field widening and minimize aberrations in the high-resolution dispersion plane of the gratings ($G_{1,2}$). As indicated in the upper inset diagram, and described in the text, both gratings are rotated to the user-set Littrow angle θ_0, and one is tilted by angle α.

Gratings replacing mirrors in this Michelson-like interferometer setup create a Fizeau fringe interference pattern, localized near the plane of the coincident grating images. Fringes corresponding to wave numbers $\sigma = \sigma_0 \pm \delta\sigma$ are spatially heterodyned about the user-set Littrow wave number σ_0. Light at wave number σ_0 produces spatial fringes with zero frequency. For gratings rotated about the vertical axis in Figure 2 (see inset), at user-set Littrow angle θ_0, all other frequencies of light ($|\sigma - \sigma_0| > 0$) produce vertically oriented fringes at corresponding spatial frequencies.

Ambiguity between positive and negative spatial frequencies in the 2-D Fourier transform (FT) is eliminated by slightly cross-tilting one grating, breaking the symmetry of the cosine term in equation (1) and *rotating* fringes proportionally to this cross-tilt angle, α. This angle is shown in Figure 2 upper inset. Note that for clarity this diagram designating α and θ_0 has been rendered with an unfolded 45° beam splitter (B.S.) angle, and no field-widening prisms are shown. Our instrument model shown in Figure 2 uses a 30° B.S. angle (and shows each full path with prism placements).

This fringe pattern (i.e., the interferogram) is recorded by CCD for further Fourier transform (FT) image processing; processing and reduction techniques are described in section 5. An example Galactic interferogram (and its FT) is shown in Figure 3, as well as a geocoronal H_α interferogram (and its FT) for comparison. Note that the Galactic emission, ~230 R from NGC1499, is well resolved, as evidenced by the narrow interferogram envelope, while the geocoronal H_α emission, ~ 9 R, is just barely resolved (broader envelope). Fringes produced by spectrally narrow calibration lines from a calibration lamp (not shown) extend to the edges of the interferogram.

The recorded fringe amplitude is a convolution of the spectral density, $B(\sigma)$, and instrumental profile, $A(x, y, \sigma)$, a nearly frequency-independent line-shape envelope function. A prefilter and CCD pixel spacing limit the
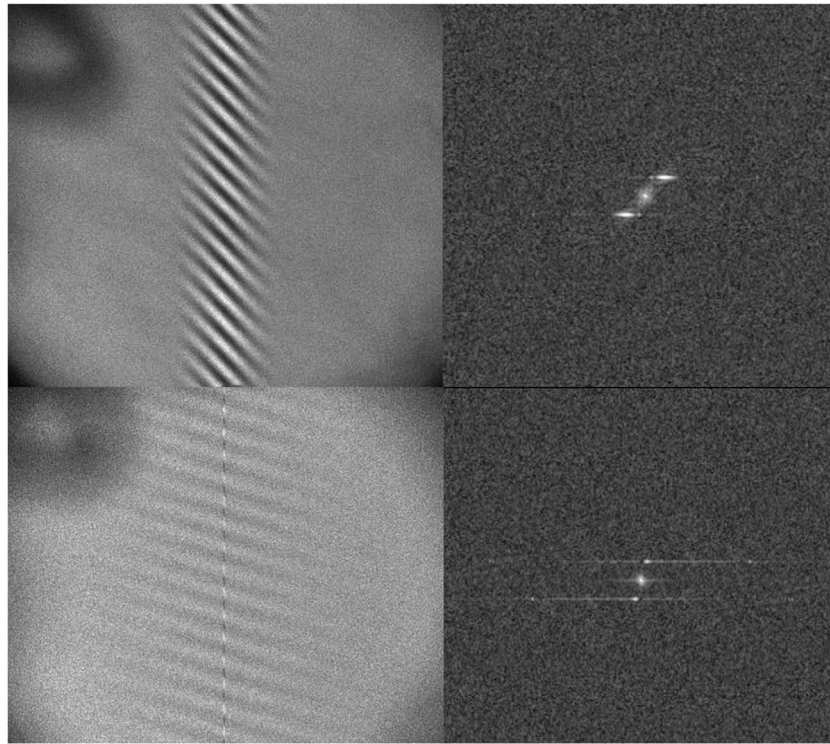
Figure 3. (top left) 392×350 pixel FW-SHS fizeau-fringe interferogram of well-resolved H_α emission from NGC1499 obtained 22 February 2014 from PBO, showing selected region to be fourier transformed. (top right) FT symmetry is broken by a small grating cross tilt (a tilt perpendicular to the dispersion plane), so the NGC1499 spectrum (Figure 4) can be obtained from the lower half plane cut through the 2-D power spectrum. (bottom left) FW-SHS fizeau-fringe interferogram of resolved geocoronal H_α emission, obtained 22 February 2014 from PBO, note the siderostat cable shadow (Figure 3, top left) is made negligible by apodization (see text). (bottom right) FT "rows" are clearly evident and contain identical information by symmetry of equation (1). The geocoronal H_α spectrum also shows an OH airglow line at a much higher frequency.

spectral range admitted and observed. For our two-dimensional format, *Roesler and Harlander* [1990] explicitly derive and show the *modulated* spatial fringe intensity can ideally be described by

$$I(x,y) = \int A(x,y,\sigma) \; B(\sigma) \; \cos[2\pi(\sigma' \; 4\tan(\theta)x + \sigma\alpha y)]\mathrm{d}\sigma \qquad (1)$$

where $\sigma' = (\sigma - \sigma_0)$; the difference is the heterodyned wave number in the dispersion dimension (x). Here (x,y) coordinates refer to recorded image orientation on the CCD.

The Fourier transform of the interferogram shows three distinct locations (rows) of power in the FT plane. Referring to Figure 3, the high-resolution spectrum is obtained by a horizontal (x) cut through the lower half (or upper) power spectrum's row, at $F_y = |F(\alpha)|$, across the region of power to the lower (or upper) left (right), at F_y, $F_x = \pm F(\alpha)$, $\pm F(\sigma')$ spatial frequency. The resulting Galactic NGC1499 spectrum is shown in Figure 4 of section 5. The central region of power (at F_y, $F_x = 0$, 0 spatial frequency) in the power spectrum is avoided by the cross-tilt angle α and can be ignored. This power is the result of incomplete flat fielding and DC subtraction, i.e., the *nonmodulated* portion of the interferogram, discussed in section 5.1; for further discussion see *Englert et al.* [2006].

Matched pairs of field-widening prisms mounted in each arm allow more off-axis rays to be measured without loss of fringe contrast, increasing the throughput of the interferometer by a factor of ~100; see *Harlander et al.* [1992] for more theoretical discussion of general field widening in SHS systems. Thus, the prisms' advantage here is that our input aperture can be opened significantly with minimal broadening of the instrumental line shape profile and centroid drift regularly associated with aperture opening in a

traditional FT spectrometer. This allows very precise Doppler shifts from faint emission at H_α to be registered across the entire band pass.

Harlander et al. [1992] show that the theoretical resolving power of a basic SHS system is as follows:

$$R_T = 4W\sigma\sin(\theta) \tag{2}$$

where W is the grating width (here 4.2×4.2 cm, 600 grooves/mm), σ is H_α wave number (15236.93 cm^{-1}), and θ is the grating Littrow angle at H_α (23.19°). Our system has a theoretical resolving power of ~100,000. The achieved FW-SHS resolving power after apodization and field widening is ~67,000 at H_α. At full sensitivity and gain, our FW-SHS can detect single Rayleigh H_α emission brightness from 1.8° FOV sources in about 10 min at a peak SNR on the order of 50 with optimal observing conditions (described in section 4). The 14 Å band pass (640 km/s at H_α) has a resolution limit of ~4.4 km/s, and with 5 times oversampling, a dispersion of ~0.539 km/s per FT pixel bin.

Because the fringes are imaged spatially and each detector element sees light from one small area through the optical train, fringe phase distortions and line shape errors can be corrected postacquisition and optical components can have relatively modest tolerances for flatness defects (as compared to Fabry-Perot instruments). Phase distortion arising from exit optics and beam splitter aberrations is minimal in our interferometer, and the instrumental profile obtained from the fringe envelope function is quite stable. For thorium calibration lines near Littrow wavelength where H_α was tuned, the phase distortion across the detector was found to be less than a fringe at all path-length differences, even near the interferogram edges. *Englert et al.* [2004] describe mathematical details of SHS distortion correction.

In our FW-SHS the spectral noise is dominated by photon noise multiplexed from the target source; photon shot noise from each spectral element sampled in the band pass is distributed across the entire interferogram. The amplitude of SHS "white" noise in spectra can be estimated from the "off rows" where no power is concentrated. We estimate (in section 8) the noise present by taking the RMS. value of FT off rows |B| (where no amplitude, B, from signal is present in the 2-D FT by virtue of the grating cross-tilt angle) as a representation of the local white noise in our spectra.

A second notable source of spectral noise, "ringing," occurs as a penalty of the finite domain of the transform across the interferogram and can be systematically reduced (at the expense of resolution) by the user's choice of apodization function. Hanning functions have been typically used for SHS airglow spectroscopy. We systematically optimized this cosine windowing function's envelope width to result in ringing amplitudes less than that of white noise, at a resolution of 67,000. For further general discussion see *Davis et al.* [2001].

4. Observing at PBO

FW-SHS geocoronal airglow observations were conducted over a two year period (2013 and 2014) at Pine Bluff Observatory (PBO, at 43.07°N, 270.33°E). Geocoronal and Galactic H_α observations, mostly obtained by FPI, have been conducted at PBO observing facilities for several decades.

The FW-SHS was coupled via fold mirror to a siderostat giving a 1.8° field of view (FOV) target on the sky. Exospheric geocoronal emission is subject to the same atmospheric extinction as Galactic emission; the siderostat's sky tracking accuracy (±0.1 arc min) allowed use of seasonally available nebular sources to correct for atmospheric extinction by the traditional Beer-Lambert approximation. To minimize scattered sunlight, clear weather observations were conducted with solar and lunar depression angles greater than 5°.

Geocoronal airglow observations towards regions of low Galactic H_α emission (usually high Galactic latitudes, $b > 30$) allow the FW-SHS to observe geocoronal H_α at a sufficient peak SNR ≈ 50 in about 10 min of CCD integration time. Brighter Galactic regions, near the plane of the Galaxy, could also be targeted for geocoronal observations provided that a sufficient Doppler shift of Galactic H_α emission is obtained to adequately separate and characterize the geocoronal H_α emission.

5. FW-SHS Signal Processing

The FW-SHS is inherently a Fourier transform instrument. A suite of reduction routines were developed in Interactive Data Language (IDL, v9.6) to FT the geocoronal data and are available upon request. Here we give

a brief outline of the reduction pipeline applied to the double-sided FW-SHS interferograms, followed by our line fitting description, and signal-to-noise definitions.

5.1. Data Reduction

FW-SHS geocoronal interferograms were integrated on a 512×512 pixel CCD. Cooling to $-100°C$ minimized dark current. For the effective interferogram size on the CCD, 392×350 pixels are selected for further processing of each interferogram image. A CCD bias image is subtracted, and each interferogram is then filtered for cosmic rays. Next, a flat-field image is divided into the interferogram. The flat-field image is constructed by summing continuum images taken with a white light source illuminating the aperture, while each interferometer arm is alternatingly blocked. This "balanced arm" approach [*Englert and Harlander*, 2006] measures the nonmodulated part of the SHS interferogram.

After flat fielding, the median interferogram value is subtracted to reduce the DC term in the Fourier transform, and the interferogram is then zero-padded (×5), oversampling the FT for more accurate fitting. The interferogram is apodized using a generalized Hanning function to give a resolving power at H_α of ~67,000. This processed interferogram is fast Fourier transformed, and a row cut through the 2-D power spectrum (the modulus of FT) in the lower half plane gives the spectrum; the upper half plane, by virtue of the grating cross-tilt angle, gives identical spectral information and is ignored. Lastly, emission spectra are corrected for the instrumental H_α filter response by dividing the spectrum through by a smoothed continuum spectral response obtained from a white light source. The white light source is collimated through the input aperture, labelled "A," shown in Figure 2. The smoothed continuum spectral response function is illustrated in Figure 4 by overplotted blue dashes.

5.2. H_α Line Profile Fitting

Spectra at this point are now ready to be fit using our VoigtFit (VF) model, a macropackage developed by R. C. Woodward (personal communication, 2013). The VF model is a least squares chi-minimization analysis program that allows multiple Voigt profiles (and background) to be fit to one dimensional data. In particular, VF allows each Voigt line parameter (e.g., width, area, and center) to be constrained (linked) to other Voigt lines (e.g., line intensity *ratios* can be held constant in the model fit to the data). In our application, at *these* shadow altitudes and resolutions, Gaussian model components are sufficient to fit the H_α profile˙s emission. Experimentally determined instrumental profiles are convolved with the model fit, such that empirical data parameters may be retrieved.

Geocoronal H_α emission spectra are fit in VF using *Meier*˙s [1995] atomic parameters to link H_α fine-structure components˙ relative areas, widths, and centers (see also *Meier* [1996]). A first fit cluster links the two solar Lyman β excited (direct) fine structure transition˙s $(3P \rightarrow 2S)$ *relative* intensities. A second fit cluster links fine structure cascade transition intensities similarly. The cascade (to total) intensity ratio has been fixed to *Roesler et al.*˙s [2014] empirically determined value of 4.5% for the observational shadow altitudes probed here.

Galactic H_α emission in geocoronal spectra are accounted for in our VF models by constraining the *relative* intensities and Doppler shifts for Galactic components present in each observation using data from WHAM˙s Northern Sky Survey [*Haffner et al.,* 2003]. Galactic component intensity ratios were determined by flux weight averaging intensities already sampled by WHAM to our FW-SHS˙s larger FOV.

Figure 3 shows the interferogram (and 2-D FT) of an FW-SHS observation towards NGC1499, reduced as just described. The resulting fit to the FW-SHS spectrum is shown in Figure 4, where the red trace represents the cascade + Galactic model fit to the (black trace) data; (blue dotted) residuals have been plotted to the same scale, but downshifted for clarity. The inset in Figure 4 shows the retrieved geocoronal H_α line after Galactic background subtraction, illustrating the grasp of FW-SHS˙s spectral baseline to fully sample and separate geocoronal and Galactic H_α emission. Note that the dispersion is negative (spectrum goes from red to blue).

In Figure 4, Galactic H_α intensity from NGC1499 is ~230 R, and geocoronal H_α intensity is ~9 R. In addition to sampling well-resolved H_α emission between the Galaxy and geocorona, the FW-SHS samples OH airglow emission (originating near 120 km altitude).
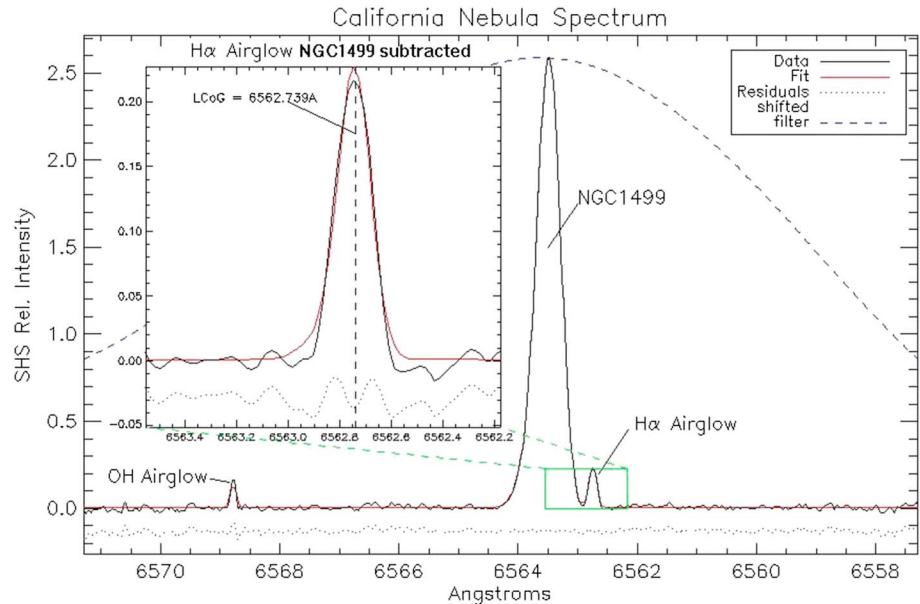
Figure 4. A 2 min H_α FW-SHS exposure, at 1.8° FOV, toward NGC1499 obtained 02/22/14 (vlsr + 35.5 km/s) showing geocoronal H_α well resolved from Galactic background. Data have been fit with the red trace, described in section 5 of text (black curve). The filter response to broad spectrum white light source is overplotted in dashed blue. (inset) FW-SHS resulting H_α airglow spectrum with Galactic background removed, confined to PBO FPI spectral range (green box, ~0.75 Å.

6. Photometric Calibration

A traditional H_α calibration target used to calibrate both WHAM and PBO FPI, is NGC7000 (i.e., the North American Nebula). Using standard stellar sources, *Scherb* [1981] calibrated a 0.8° FOV portion of NGC7000, centered at right ascension and declination, $\alpha(1950) = 20^h\ 56^m\ 17^s$, $\delta(1950) = 44°\ 24'\ 03''$, with H_α surface brightness of 850 ± 50 R. Using WHAM's FPI (spectral baseline ~200 km/s at H_α), *Haffner et al.* [2003] calibrated the same NGC7000 look direction at a 1.0° FOV with H_α surface brightness of 800 ± 50 R (NGC7000 is *not* spatially uniform). Using the FPI at PBO (spectral baseline ~75 km/s at H_α), *Mierkiewicz et al.* [2006] extended the photometric calibration of NGC7000 to a FOV of 1.4° with H_α surface brightness of ~650 R. By targeting the same patch of sky at alternating FOV's, the FW-SHS photometric response can be obtained by similarly bootstrapping to a 1.8° FOV. FW-SHS data for this direct calibration method are currently being reduced (not presented here).

Since NGC7000 is not always available, we developed an alternative nightly calibration method using existing Galactic H_α data from WHAM. Galactic regions of known H_α intensity were targeted that spatially fill the FW-SHS FOV as uniformly as possible. The photometric response of the FW-SHS instrument to H_α emission could then be statistically estimated using WHAM's Northern Sky Survey database by geometrically weighting the Galactic H_α flux sampled by WHAM towards the same look direction within the FW-SHS larger FOV.

Flux-weighted calculations of intensity reproduced all above listed intensities for NGC7000 at varying FOVs, within ± 50 R. Thus, Galactic H_α emission in an FW-SHS spectrum could be reliably estimated to provide a useful photometric calibration of the geocoronal H_α emission:

$$I_{SHS} \cong \frac{1}{'\Omega_{SHS}} \Sigma_i I_i' \Omega_i + \varepsilon \tag{3}$$

where $I_i'\Omega_i$ is the partial flux of each 1° WHAM beam sampled within $'\Omega_{SHS} = 1.8°$ FOV of the FW-SHS; here ε is the flux-weighted error approximation for FOV within FW-SHS observation not directly sampled by WHAM. It can be estimated as the average flux of the WHAM beams sampled, multiplied by the FOV ratio, $'\Omega_{not\ sampled}/'\Omega_{sampled}$. The geometric illustration of equation (3) is shown in Figure 7, discussed in section 8.

The FW-SHS was also directly cross calibrated with the already calibrated PBO FPI. *Mierkiewicz et al.* [2006] demonstrated the absolute photometric response of the PBO FPI to the near spatially uniform geocoronal

H_α emission, so the FW-SHS response could be directly obtained by comparing geocoronal H_α emission line areas. Zenith H_α observations were obtained simultaneously by PBO FPI and FW-SHS during the summer and fall of 2014 for this purpose and to also validate the WHAM data calibration method via equation (3) above.

7. Spectral Calibration

A Thorium Argon (ThAr) hollow cathode calibration lamp was used each observing night to spectrally register geocoronal H_α emission and to calibrate the FW-SHS dispersion. Hourly ThAr was needed to register sky spectra due to slow room temperature fluctuations inducing small grating and exit optic thermal shifts in our open air interferometric setup. The resulting spectral shifts of ThAr line peaks between successive spectra, across a few resolution elements, were linearly interpolated through time to retrieve absolute peak spectral positions in geocoronal observations taken between lamp readings.

FW-SHS gratings were tuned so that the H_α emission (6563 Å) fell within a few angstroms of the Littrow wavelength. Across the filter-corrected 14 Å band pass, five thorium emission lines were then available for dispersion calculation (6558, 6560, 6564, 6565, and 6569 Å). Thorium emission at typical hollow cathode lamp temperatures ~1000 K has an estimated line width of 0.4 km/s [*Mierkiewicz et al.,* 2006], an order of magnitude lower than the FW-SHS resolution limit (~4.4 km/s is the FW-SHS observed width of ThAr 6564 Å emission line, with apodization). Thus, Thorium emission can be used as an effective delta-function input to retrieve the FW-SHS instrumental profile (IP). The 6564 Å Thorium emission line, nearest the Littrow wavelength and H_α, was used as the true IP. This symmetric IP was convolved in the fitting of geocoronal H_α spectra to differentiate true H_α emission width from instrumental broadening.

The magnitude of errors in fitted spectral line positions, in absence of thermal drifts, give our FW-SHS an estimated Doppler shift detectability limit on the order of 100 m/s. *Davis et al.* [2001] remind us Fourier transform spectrometer instruments in the photon noise-dominated applications can theoretically achieve uncertainties in spectral line positions roughly equal to the ratio of the $\mathrm{FWHM}/(\mathrm{SNR}_\sigma \times \sqrt{N_S})$. For example, with average H_α line width (FWHM) of ~5.5 km/s, a peak SNR on the order of 50, and a minimally sampled number of points in the line width, $N_s \sim 6$, gives an estimate of the Doppler shift detectability to an order of 50 m/s.

8. First Light Results

Coincident geocoronal observations by the PBO FPI and FW-SHS were conducted to assess instrumental performance, demonstrating the FW-SHS utility for geocoronal research. Figure 4 illustrated the FW-SHS spectral baseline grasp of the entire Galactic background; narrower spectral baseline instruments designed for geocoronal H_α observations, e.g., the PBO FPI, must rely on extrapolation outside their band pass to fit large redshifted Galactic H_α components.

To compare the PBO FPI and FW-SHS coincident observations between geocoronal spectra, we use a local (peak) signal-to-noise ratio (SNR) estimate in the spectral domain. *Davis et al.* [2001] and *Harlander* [1991] show that the local SNR for a Fourier transform instrument can be estimated as follows:

$$\frac{s}{N_\sigma} = \frac{B(\sigma)}{\in_\sigma} \tag{4}$$

where $B(\sigma)$ is the peak signal in the spectral domain and $\in$ is the RMS noise (refer to section 3).

Mierkiewicz et al. [2006] and *Coakley et al.* [1996] show that the local SNR ratio for a Fabry-Perot system can be estimated as follows:

$$\frac{S}{N_{\mathrm{est}}} = \frac{Lcp}{\sqrt{Lcp + Bcp + DTp + R_n^2 p}} \tag{5}$$

where L is the recorded number of analog-to-digital (ADU) counts per pixel on the line (multiplied by 0.8, the average line transmittance within FWHM), B is the background ADU, recorded in time T in seconds, at an effective gain of c (photoelectrons/ADU), and p is the number of pixels annularly summed into one resolution element (or bin). D and R are the measured dark current and RMS read noise.

Figures 5 and 6 show 10 min coincident zenith observations from the FW-SHS and PBO FPI, respectively, taken at the same time near local midnight on 22 September 2014 (at an observational shadow altitude of
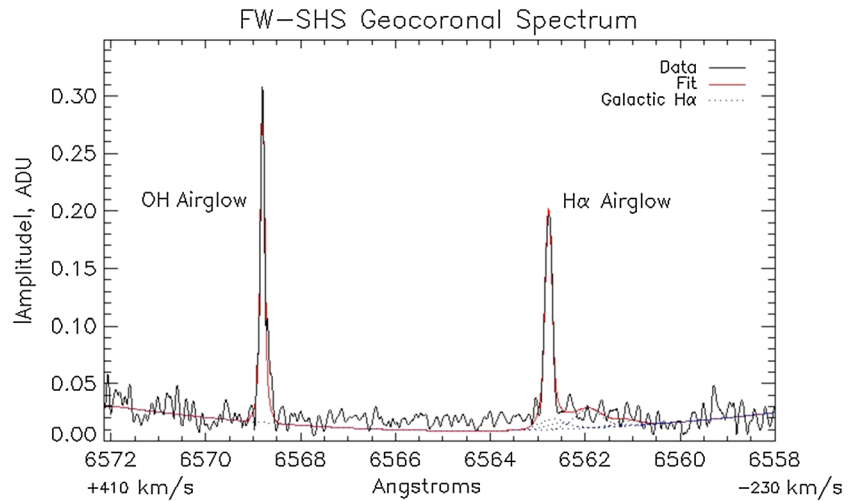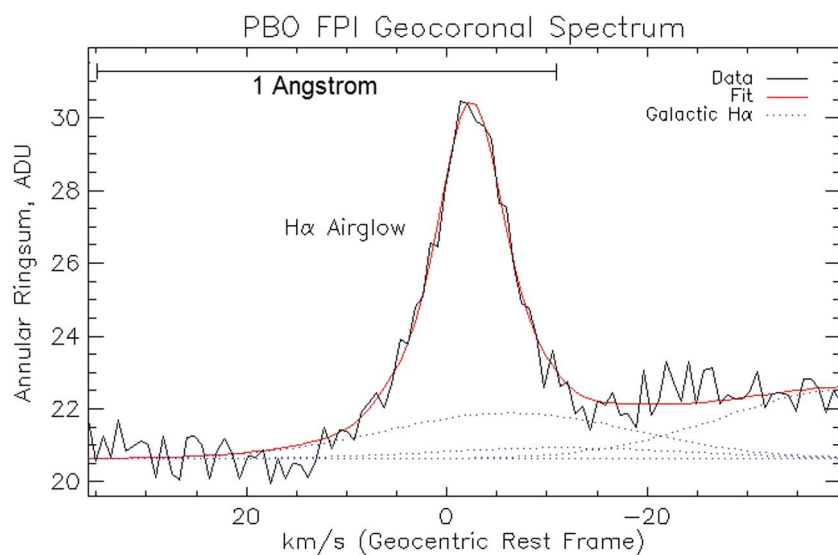
Figure 5. Geocoronal spectrum from the FW-SHS. Using the already calibrated PBO-FPI's response to the geocoronal H_α emission, or by using the calibrated WHAM Galactic H_α emission, the FW-SHS observed H_α emission intensity can be determined. Both FW-SHS and PBO FPI agree that the geocoronal Doppler emission width is 4.9 km/s, a typical value for this observational shadow altitude (3100 km).

3100 km, and vlsr = −29.7 km/s). Black traces are data, red solid traces are the retrieved fits, and overplotted dashed blue traces are WHAM-derived Galactic components included in the fits [*Haffner et al.,* 2003].

Referring to equation (5) and Figure 6, our PBO FPI's CCD operates at $c = 1.22$ photoelectron/ADU, $R_n = 7$ e$^-$/pixel, and $D = 0.001$ e$^-$/pixel/s. The PBO FPI geocoronal H_α spectrum was retrieved by annularly summing the observed ring image obtained on CCD [*Coakley et al.,* 1996]; $p = 336$ pixels were summed into the resolution element at the geocoronal line peak. At an integration time of 600 s, the signal-to-noise in the peak of the geocoronal line is ≈ 53.

Referring to equation (4) and Figure 5, our FW-SHS CCD operates at a lower read noise (4.8 e$^-$/pixel), higher gain (1.42 photoelectron/ADU), and similar dark current as the PBO FPI CCD, but all negligible

Figure 6. Coincidently obtained PBO FPI spectrum. Using the already calibrated PBO-FPI's response to the geocoronal H_α emission, or by using the calibrated WHAM Galactic H_α emission, the FW-SHS observed H_α emission intensity can be determined. Both FW-SHS and PBO FPI agree that the geocoronal Doppler emission width is 4.9 km/s, a typical value for this observational shadow altitude (3100 km).
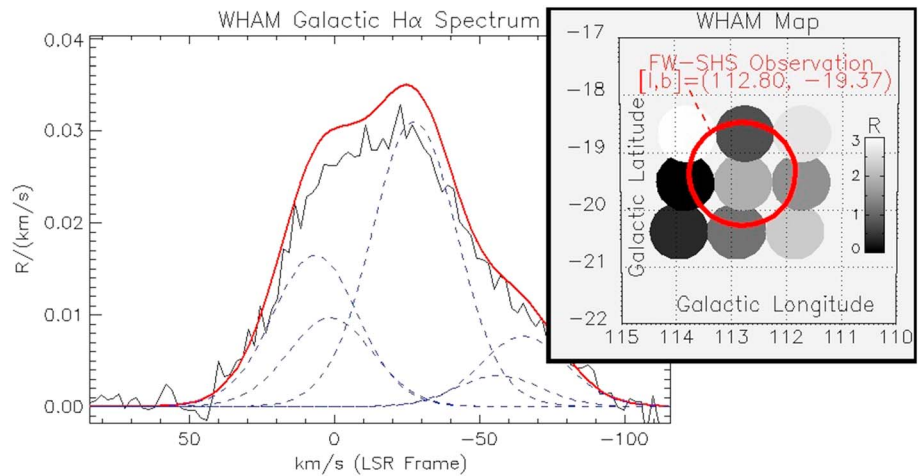
Figure 7. WHAM spectrum of Galactic H_α emission for look direction coincidently probed by FW-SHS and PBO FPI (Figures 5 and 6). The black trace is the average raw Galactic spectrum of each WHAM beam sampled near the coincident observation's Galactic coordinates. The red trace is a more accurate, flux-weighted spectral estimate (by equation (3)), accounting for spatial variation of each WHAM beam's components within our FW-SHS's larger FOV (overplotted red circle on inset WHAM map of 1° FOV intensities, projected on normalized grey scale). The Galactic component comprising the red trace are overplotted with blue dashes.

since we are dominated by photon multiplexed noise. The RMS white noise level in this FW-SHS spectrum was 0.0135 ADU. At an integration time of 600 s, the signal-to-noise in the peak of the geocoronal line is ≈ 16.

The relatively lower peak SNR in the FW-SHS observation, as compared to the PBO FPI coincident observation (shown in Figures 5 and 6), suggests the PBO FPI instrument can better determine cascade components in the wings of the geocoronal line; however, contamination by unaccounted Galactic components extending the PBO FPI spectral baseline can introduce systematic errors to geocoronal line profile fits. The FW-SHS, on the other hand, can obtain dispersion and line center precisions (100 m/s, discussed in section 7) across a baseline (~10 times longer than the PBO FPI) capable of fully fitting Galactic emission, suggesting that it is better suited for determining geocoronal line center shifts. Noise could be further reduced in the FW-SHS spectra by use of a narrower input filter (e.g., blocking the OH signal) and smoother FT apodization functions, but at the expense of resolution.

WHAM data for this look direction coincidently probed by FW-SHS and PBO FPI (Figures 5 and 6) suggests that there are several faint (<1 R) and wide (~40 km/s) Galactic H_α emission components near the geocoronal H_α emission. Referring to the inset WHAM map in Figure 7, equation (3) predicts Galactic H_α intensity ≈ 2.6 R. The complete Galactic component's background emission is evident in the FW-SHS spectrum but only partially seen by the shorter spectral baseline of the PBO FPI. Thus, in this example spectrum the PBO FPI *overestimates* the Galactic H_α intensity (here by a factor of ~2.46) when extrapolating WHAM-derived fit components beyond the available spectral range.

The well-calibrated PBO FPI intensity response suggests the geocoronal H_α emission intensity coincidently observed by the FW-SHS was 3.7 R—an expected value for the observational shadow altitude probed. In our FW-SHS spectrum, cross multiplying the total Galactic fit area by the ratio of the PBO FPI calibrated geocoronal emission to FW-SHS geocoronal area, R/area, suggests the FW-SHS observed Galactic background is 2.8 R—nearly identical to what WHAM predicts (2.6 R).

This implies that the observed FW-SHS geocoronal emission intensity can be determined reasonably well using background Galactic H_α emission already present in the FW-SHS spectrum and WHAM data alone (via equation (3)). The WHAM-derived predicted geocoronal H_α intensity observed by the FW-SHS is 3.4 R. The small difference (0.3 R) from what the PBO FPI predicts for the geocoronal intensity is likely due to noise affecting fits and also possibly spatial nonuniformity of surface brightness emission in the actual observed Galactic region, as compared to the WHAM data estimate based on 1° FOV sampling (see Figure 7, inset map).
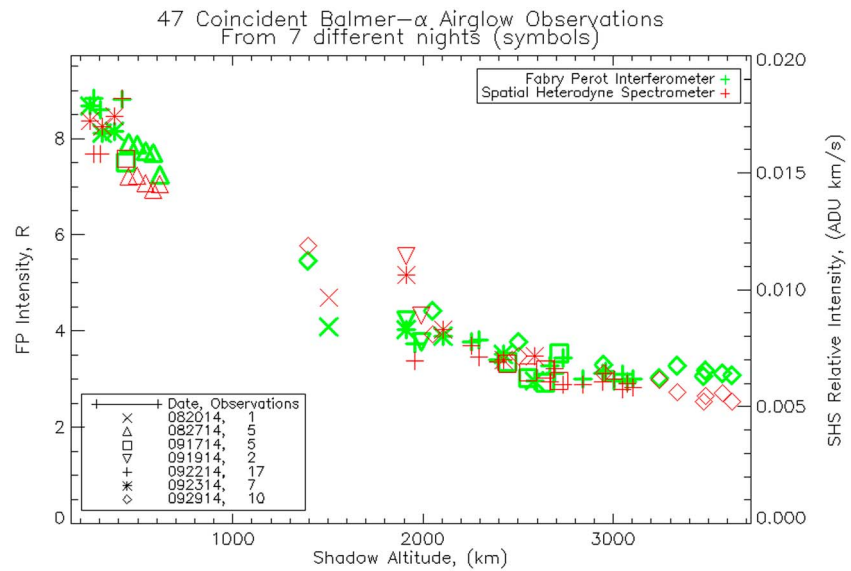
Figure 8. FW-SHS observations of geocoronal H_α airglow intensity (red) versus viewing geometry (i.e., shadow altitude) show relative response agreement with coincidently obtained PBO FPI (green) observations. Intensities were obtained by integrating emission 10 km/s around geocoronal peaks in both instrumental spectra, and *assuming* negligible (flat) Galactic H_α emission.

A collection of coincident PBO FPI and FW-SHS zenith observations, with low Galactic emission, allows a geocoronal cross-calibration curve of (known PBO FPI) emission intensity versus shadow altitude to be constructed; this is shown in Figure 8. Intensities were obtained by integrating emission ± 10 km/s around geocoronal peaks in both instrument's spectra, and *assuming* negligible (flat) Galactic background. As anticipated, the FW-SHS (red points) shows good relative agreement in photometric response with the PBO FPI (green points). Knowing the absolute photometric response of the PBO FPI, the FW-SHS photometric response at H_α can be retrieved.

From previously obtained and calibrated PBO FPI data [*Mierkiewicz et al.*, 2006], geocoronal H_α airglow is known to fall from 12 (± 3) R and plateau near ~2 R across the plotted range of shadow altitude. The break in Figure 6 data, between ~1000 and 2000 km shadow altitudes, is due to Galactic plane passing overhead during coincident zenith observations conducted in fall of 2014; those geocoronal data points could not be simply reduced with a constant background assumption. But as previously described with Figures 3 and 4, careful component fitting of this Galactic H_α emission can provide additional photometric calibration via the WHAM data set itself.

9. Conclusions

In this paper first light results were presented illustrating the FW-SHS interferometer's performance investigating geocoronal H_α emission. Emission as faint as a single Rayleigh can be observed within 10 min at a spectral resolving power near to, and sensitivity typical of, FPI's used for geocoronal work. In particular, the FW-SHS instrument's relatively long spectral baseline allows better characterization of background Galactic H_α emission in geocoronal spectra, as well as a robust spectral calibration to register sky spectra.

We also showed that the WHAM Galactic data can be used to calibrate the terrestrial hydrogen airglow observations taken by the FW-SHS instrument and validated this by cross comparison with the already calibrated PBO FPI. This method can be applied to the calibration of H_α observations made with other interferometers, especially during times of the year when the standard North American Nebula source is not observable or when the instrument does not have pointing capabilities to observe nebular sources. The uncertainty in this photometric calibration method (using WHAM data alone) is ultimately determined by the FW-SHS obtained SNR in each observation and the uncertainty in the WHAM data itself (~10%, approximately). Additionally, the agreement of the FW-SHS observed geocoronal intensity as derived by

either coincident PBO FPI geocoronal observation or WHAM Galactic data (constraining Galactic emission in the FW-SHS spectra) corroborates the two independent calibration methods used for WHAM and the PBO FPI.

Since the FW-SHS is a table top-sized instrument and can be easily transported in the field, it is currently being redeployed from PBO to Daytona Beach, Florida (ERAU). This FW-SHS will be integrated along with a suite of SHS and FPI instruments in a new, remotely operable and transportable optical observatory for investigations of near space weather and upper atmospheric airglow phenomena.

References

Bishop, J. (2001), Thermospheric atomic hydrogen densities and fluxes from dayside Lyman α measurements, *J. Atmos. Sol. Terr. Phys.*, *63*, 331–340, doi:10.1016/S1364-6826(00)00211-X.

Bishop, J., E. J. Mierkiewicz, F. L. Roesler, J. F. Gomez, and C. Morales (2004), Data-model comparison search analysis of coincident PBO Balmer α, EURD Lyman β geocoronal measurements from March 2000, *J. Geophys. Res.*, *109*, A05307, doi:10.1029/2003JA010165.

Coakley, M. M., F. L. Roelser, R. J. Reynolds, and S. Nossal (1996), Fabry-Perot/CCD annular summing spectroscopy: Study and implementation for aeronomy applications, *Appl. Opt.*, *35*, 6479–6493, doi:10.1364/AO.35.006479.

Corliss, J. B., W. M. Harris, E. J. Mierkiewicz, and F. L. Roesler (2015), Development and field tests of a narrowband all-reflective spatial heterodyne spectrometer, *Appl. Opt.*, *54*(30), 8835–8843, doi:10.1364/AO.54.008835.

Davis, S. P., M. C. Abrams, and J. W. Brault (2001), *Fourier Transform Spectrometry*, Academic Press, San Diego, Calif.

Englert, C. R., and J. M. Harlander (2006), Flatfielding in spatial heterodyne spectroscopy, *Appl. Opt.*, *45*(19), 4583–4590, doi:10.1364/AO.45.004583.

Englert, C. R., J. M. Harlander, J. G. Cardon, and F. L. Roesler (2004), Correction of phase distortion in spatial heterodyne spectroscopy, *Appl. Opt.*, *43*(36), 6680–6687, doi:10.1364/AO.43.006680.

Haffner, L. M., R. J. Reynolds, S. L. Tufte, G. J. Madsen, K. P. Jaehnig, and J. W. Percival (2003), The Wisconsin H-alpha mapper northern sky survey, *Astrophys. J. Suppl.*, *149*(2), 405–422, doi:10.1086/378850.

Harlander, J. M. (1991), Spatial heterodyne spectroscopy: Interferometric performance at any wavelength without scanning, Ph.D. thesis, Univ. of Wisconsin-Madison, Madison.

Harlander, J. M., R. J. Reynolds, and F. L. Roesler (1992), Spatial heterodyne spectroscopy for the exploration of diffuse interstellar emission lines at far ultraviolet wavelengths, *Astrophys. J.*, *396*, 730–740, doi:10.1086/171756.

Kerr, R. B., S. K. Atreya, J. W. Meriwether, C. A. Tepley, and R. G. Burnside (1986), Simultaneous H a line profile and radar measurements at Arecibo, *J. Geophys. Res.*, *91*, 4491–4512, doi:10.1029/JA091iA04p04491.

Kerr, R. B., et al. (2001), Periodic variations of geocoronal Balmer-alpha brightness due to solar-drive exospheric abundance variations, *J. Geophys. Res.*, *106*, 28,797–28,817, doi:10.1029/1999JA900187.

Lawler, J. E., Z. E. Labby, J. M. Harlander, and F. L. Roesler (2008), Broadband, high-resolution spatial heterodyne spectrometer, *Appl. Opt.*, *47*(34), 6371–6384, doi:10.1364/AO.47.006371.

Meier, R. R. (1995), Solar Lyman series line profiles and atomic hydrogen excitation rates, *Astrophys. J.*, *452*, 462–471, doi:10.1086/176318.

Meier, R. R. (1996), Solar Lyman series line profiles and atomic hydrogen excitation rates, with Erratum, *Astrophys. J.*, *468*, 455, doi:10.1086/177705.

Mierkiewicz, E. J., F. L. Roesler, S. M. Nossal, and R. J. Reynolds (2006), Geocoronal hydrogen studies using Fabry-Perot interferometers, part 1: Instrumentation, observations, and analysis, *J. Atmos. Sol. Terr. Phys.*, *68*, 1520–1552, doi:10.1016/j.jastp.2005.08.024.

Mierkiewicz, E. J., F. L. Roesler, and S. M. Nossal (2012), Observed seasonal variations in exospheric effective temperatures, *J. Geophys. Res.*, *117*, A06313, doi:10.1029/2011JA017123.

Nossal, S. M., R. J. Reynolds, F. L. Roesler, and F. Scherb (1993), Solar cycle variations of geocoronal Balmer α emission, *J. Geophys. Res.*, *98*, 3669–3676, doi:10.1029/92JA02568.

Nossal, S. M., F. L. Roesler, and M. M. Coakley (1998), Cascade excitation in geocoronal hydrogen Balmer-α line, *J. Geophys. Res.*, *103*, 381–390, doi:10.1029/97JA02435.

Nossal, S. M., F. L. Roesler, R. J. Reynolds, M. Haffner, S. Tufte, J. Bishop, J. Percival, and E. J. Mierkiewicz (2001), Geocoronal Balmer a intensity measurements using the WHAM Fabry-Perot facility, *J. Geophys. Res.*, *106*, 5605–5616, doi:10.1029/2000JA000003.

Nossal, S. M., E. J. Mierkiewicz, F. L. Roesler, R. J. Reynolds, and L. M. Haffner (2006), Geocoronal hydrogen studies using Fabry-Perot interferometers, part 2: Long-term observations, *J. Atmos. Sol. Terr. Phys.*, *68*, 1553–1575, doi:10.1016/j.jastp.2005.08.025.

Nossal, S. M., E. J. Mierkiewicz, F. L. Roesler, L. M. Haffner, R. J. Reynolds, and R. C. Woodward (2008), Geocoronal hydrogen observations spanning three solar minima, *J. Geophys. Res.*, *113*, A11307, doi:10.1029/2008JA013380.

Roesler, F. L., and J. M. Harlander (1990), Spatial heterodyne spectroscopy: Interferometric performance at any wavelength without scanning, *Proc. SPIE*, *1318*, 234–243.

Roesler, F. L., J. M. Harlander, J. G. Cardon, C. R. Englert, R. J. Reynolds, K. Jaehnig, S. Watchorn, E. J. Mierkiewicz, and J. Corliss (2003), Spatial heterodyne spectroscopy: An emerging technology for interference spectroscopy, in *Hubble's Science Legacy: Future Optical-Ultraviolet Astronomy From Space*, ASP Conf. Ser., vol. 291, edited by K. R. Sembach et al., pp. 395–398, Univ. of Chicago, Illinois.

Roesler, F. L., E. J. Mierkiewicz, and S. M. Nossal (2014), The geocoronal Hα cascade component determined from geocoronal Hβ intensity measurements, *J. Geophys. Res. Space Physics*, *119*, 6642–6647, doi:10.1002/2014JA020026.

Scherb, F. (1981), Hydrogen production rates from ground-based Fabry-Perot observations of comet Kohoutek, *Astrophys. J.*, *243*, 644–650, doi:10.1086/158630.

Tinsley, B. (1970), Temporal variations in geocoronal Balmer alpha, *J. Geophys. Res.*, *73*, 4139–4149, doi:10.1029/JA073i013p04139.